

SUPPLEMENTARY INFORMATION

Dissipationless zero energy epigraphene edge state for nanoelectronics

*Vladimir S. Prudkovskiy^{1,2,3}, Yiran Hu², Kaimin Zhang¹, Yue Hu², Peixuan Ji¹, Grant Nunn²,
Jian Zhao¹, Chenqian Shi¹, Antonio Tejada^{4,5}, David Wander³, Alessandro De Cecco³,
Clemens B. Winkelmann³, Yuxuan Jiang⁶, Tianhao Zhao², Katsunori Wakabayashi^{7,8},
Zhigang Jiang², Lei Ma^{1,9,†}, Claire Berger^{2,3,10}, Walt A. de Heer^{1,2,*}*

¹ Tianjin International Center for Nanoparticles and Nanosystems (TICNN), Tianjin University, 92 Weijin Road, Nankai District, China, 300072

² School of Physics, Georgia Institute of Technology, Atlanta, Georgia 30332, United States

³ Institut Néel, Univ. Grenoble Alpes, CNRS, Grenoble INP, 38000 Grenoble, France

⁴ Laboratoire de Physique des Solides, CNRS, Univ. Paris-Sud, 91405 Orsay, France

⁵ Synchrotron SOLEIL, L'Orme des Merisiers, Saint-Aubin, 91192 Gif sur Yvette, France

⁶ National High Magnetic Field Laboratory, Tallahassee, Florida 32310, United States

⁷ School of Science and Technology, Kwansei Gakuin University, Gakuen 2-1, Sanda 669-1337, Japan

⁸ Center for Spintronics Research Network (CSRN), Osaka University, Toyonaka 560-8531, Japan

⁹ State key laboratory of Precision Measurement Technology and Instruments, Tianjin University, 92 Weijin Road, Nankai District, China, 300072

¹⁰ International Research Lab 2958 Georgia Tech-CNRS, 57070 Metz, France

Corresponding authors

*e-mail: walter.deheer@physics.gatech.edu

† e-mail maleixinjiang@tju.edu.cn

Methods

Non-polar wafers were produced from commercial bulk single crystal 4H-SiC rod, by cutting them along directions corresponding to the sidewall facets ($\bar{1}10n$), $n=5$.¹⁻³ The wafers were then CMP polished. Graphene samples were prepared using the Confinement Controlled Sublimation method⁴ in a graphite crucible provided with a 0.5 mm hole, under various growth conditions: Sample A (Figs 4-6) in a 1atm Ar atmosphere at 1550°C for 30 min followed by 1650°C for 2 hours; Sample B (Fig. 2B, C, E) in vacuum in a face-to-face configuration at 1550°C for 20 min; Sample C (Fig. 2D, S3), in a 1 atm Ar atmosphere at 1550°C for 30 min followed by 1650°C for 15 min. Sample A (Figs 4-6) was patterned using conventional lithography methods (Fig. 3): after graphene annealing in vacuum at 1000°C for 30 min, an alumina protecting layer (30 nm thick) was deposited on graphene by evaporating Al (0.5 Å/sec) in a $\approx 5 \times 10^{-5}$ mb oxygen atmosphere. A bilayer MMA/PMMA resist was patterned, and an additional alumina coating (20nm) was evaporated on top, resulting in the desired Hall bar shape alumina mask after lift-off. The alumina/graphene/SiC was then dry-etched in BCl₃ plasma (ICP) using the thick alumina as a mask. Buffered hydrogen fluoride was used to provide openings in the alumina for contacts. E-beam evaporated Pd/Au was used for contacts and the top-gate electrode. For further details see Ref.5.

Transport measurements were performed in a 1.6-420K cryocooler provided with a 9 Tesla magnet. Voltages were sequentially measured by eight lock-ins (frequency < 21 Hz), with low current excitation (from 1 to 10nA). Cryogenic STM images were made in high resolution AFM/STM⁶ at the CNRS Néel Institute, and at the TICNN using a RHK PanScan Freedom STM. Raman spectra were acquired with a high-resolution confocal Horiba Raman

microscope system at an excitation wavelength of 532nm. Room temperature ARPES measurements were performed at the CASSIOPEE beam line of Soleil synchrotron, equipped with a Scienta R4000 analyzer and a modified Peterson PGM monochromator with a resolution $E/\Delta E=70,000$ at 100 eV and 25,000 for lower energies. The 6 axis cryogenic manipulator is motorized. The sample was prepared ex-situ and cleaned under ultra-high vacuum conditions by flash heating it at 700°C.

The infrared (IR) magneto-spectroscopy measurements were carried out in reflection mode using a standard Fourier-transform IR spectroscopy technique (Bruker VERTEX 80v) at liquid helium temperature. The IR light from a Globar source was delivered to the non-polar epigraphene through an evacuated light pipe, and the reflected light was guided to a Si bolometer away from the magnetic field center. All measurements were performed in Faraday geometry with the field applied perpendicular to the graphene.

New quasiparticle or conventional edge state?

The EGES is a state that does not produce a Hall voltage at any gate voltage and the EGES current simply adds in parallel to the conventional graphene currents at all temperatures magnetic fields and gate voltages. These defining properties do not apply to the conventional edge state. Consequently, the EGES is not a conventional edge state.

Conductance quantization results from the exclusion principle. A conductance of $1 G_0$ is characteristic for a quasiparticle that transports a single charge. This indicates that the EGES is a singly charged, spin $\frac{1}{2}$ fermion. However, it does not produce Hall voltage, which implies that its net charge vanishes. Note that a left moving electron and a right moving hole both transport a single charge. If both occur simultaneously, the Hall voltage vanishes and the graphene ribbon segment remains uncharged in the process, but such a quasiparticle is a boson.

We therefore propose that the object is a linear combination of a forward moving electron and a backward moving hole to produce a fermion with net zero charge. The high density of states at $E=0$ pins the Fermi level. This is the charge neutrality point (Dirac point) where the hole band and electron band are degenerate. Hence it is plausible that a new quasiparticle as described above exists there.

Why is the edge state not seen in patterned exfoliated graphene?

Usual lithography processes, that typically involves oxygen plasma etching applied to graphene on BN and on SiO_2 substrates, to which the graphene is weakly adhered, is known to cause disordered edges that are insulating.⁷⁻¹⁵ Acene edges are chemically reactive¹⁶, so that if they are not stabilized or if they are functionalized^{17,18} the edge state band structure

is perturbed leaving an energy gap, or a mobility gap at $E=0$, as typically seen in patterned exfoliated graphene on BN or SiO_2 ^{7-13,19} and the edge state is not observed. Hwang et al²⁰ have produced graphene nanoribbons on polar epigraphene using a soft mask (PMMA) and oxygen plasma etching. In contrast, epigraphene devices produced in this work on neutral epigraphene, using the alumina/graphene/SiC “sandwich” and the BCl_3 ICP etching described before, produce a bulk graphene with a mean free path <10 nm (bulk mobility $\mu=750 \text{ cm}^2\text{V}^{-1}\text{s}^{-1}$) and an edge state with mfp’s exceeding $20 \mu\text{m}$. These results show that the substrate and the etching process are critical for the edge state. Sidewall ribbons are produced without lithography, by thermal annealing of sidewalls etched in SiC ($T>1300^\circ\text{C}$).^{1,2} The ribbons terminate in the SiC^{21,22} and the edge state is observed with mean free paths exceed $20 \mu\text{m}$.

Monolayer or bilayer?

A quantum Hall plateau at $R_H = \frac{1}{4} R_0$ would indicate a bilayer, not a monolayer ($R_H = \frac{1}{2} R_0$ for a monolayer at $N_{LL}=0$), and there are no other Hall features to help distinguish the two. However, the Landau level spacing $\Delta E_{LL} = E_{L1} - E_{L0}$ in a bilayer^{23,24} is $\Delta E_{LL}[\text{meV}] = 2.2 B[\text{T}]$, whereas for a monolayer $\Delta E_{LL}[\text{meV}] = 35 \sqrt{B[\text{T}]}$. Shubnikov-de Haas oscillations follow $A_{\text{Theory}}(T) = u / \sinh(u)$,^{25,26} where $u = 2\pi^2 k_B T / \Delta E_{LL}$. Experimentally, at $B=9$ T, we find for $T=[4.5, 40, 65, 150, 300 \text{ K}]$ that $A_{\text{Exp}}(T) = [1, 0.72, 0.48, 0.31, 0.07]$, respectively (Fig. 6A, 6C and Fig. S1). However, for a bilayer $A_{\text{Theory}}(T) = [0.97, 0.23, 0.05, 10^{-4}, 10^{-9}]$, which definitively disagrees with experiment. On the other hand, for a monolayer $A_{\text{Theory}}(T) = [1, 0.94, 0.85, 0.47, 0.1]$ which agrees well.

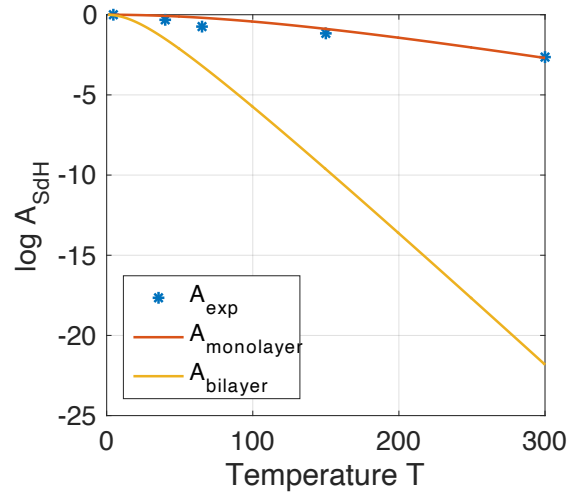


Figure S1. Measured Amplitude of the Shubnikov-de Haas oscillations as a function of temperature for segment **A** at 9 T (from Fig. 6A in the text), compared with theoretical predictions for a monolayer and a bilayer.

Magnetic induced edge states and the EGES

Quantum Hall effect

Quantized EGES transport is observed in the absence of a magnetic field, as abundantly demonstrated in the 40 nm wide sidewall graphene ribbons¹. In the wider graphene ribbons used here, at low temperatures, the junctions add an additional resistance ($\approx h/e^2$) due to weak localization in the junctions. As expected, the coherent back scattering is suppressed either by a relatively small magnetic field (≈ 2 T) or at relatively temperatures (≈ 50 K). These properties are inconsistent with the quantum Hall effect, which is quenched at higher temperatures (plateaus are observed at least up to 150 K, see Fig. 5A). More importantly, the quantum Hall effect normally manifests as a quantized Hall resistance in a magnetic field. But the EGES has no Hall effect at CNP even in large magnetic fields (see Fig.

6E) and the Hall resistance linearly increases with increasing V_G away from CNP causing non-quantized Hall plateaus. Yet the EGES longitudinal conductance is quantized. Hence, the EGES is categorically not related to the quantum Hall effect. These effects are explained in detail in the main text. It is important to note that, according to theory²⁷, the EGES requires both edges that are therefore not independent ballistic conductors. If they were, the conductance would be at least $2 G_0$, rather than $1 G_0$. Moreover, the conductances (including fluctuations) measured on opposite sides, of a ribbon are identical (see Fig. S10.).

In contrast, the quantum Hall effect requires a strong magnetic field to produce a highly protected ballistic edge from source to drain where one edge is at the potential of the source and the other at the potential of the drain, regardless of the topology of the edge. The quantum Hall effect is robust in epigraphene with insulating edges²⁸⁻³⁰. In fact, Si terminated face SiC²⁸ epigraphene Hall bars are used as ultraprecise quantum Hall standards with a precision of 3 parts per billion, which precludes any shorting effect from the edge state.^{28,29} While the large SiC induced charge on polar face epigraphene may saturate the 0-DOS peak, note that those Hall bars are produced using oxygen plasma etching and a polymer mask which causes the edge to be insulating. This clearly shows that epigraphene does show a conventional quantum Hall effect when the edges are insulating.

Lack of edge state in exfoliated graphene

The EGES transport has not been observed in exfoliated graphene, not even in unprocessed graphene flakes³¹. Instead the conventional quantum Hall effect and a variety of novel properties^{8,31,32} related to magnetically induced edge states are observed that are not

related to the EGES. In particular, a perpendicular magnetic field produces a ballistic edge state that follows the periphery of the sample from source to drain. These quantum Hall edge states are observed both in 2-point measurements and in Hall measurements. The polarity of the Hall voltage, determined by the Lorentz force, depends on whether electrons or holes carry the current. Theory predicts that in a magnetic field, the edge state will merge with the $N_{LL}=0$ Landau level³³ to produce the $R_{Hall}=\pm \frac{1}{2} R_0$ quantum Hall plateaus, depending on whether the Fermi level is positive or negative. In both cases, the 2 point resistance will be $\frac{1}{2} R_0$. These properties are also observed in polar epigraphene Hall bars.^{28,29}

Young et al.⁸ and Veyrat et al.³² demonstrated the spin-Hall effect in high mobility graphene Hall bars in BN/graphene/BN hetero-structures (typical mobilities $\mu>30,000 \text{ cm}^2\text{V}^{-1}\text{s}^{-1}$). At CNP the Hall bars on thick BN are insulating in perpendicular magnetic fields $\geq 0.75 \text{ T}$. Using very thin BN spacers on a high K dielectric for $0.5 \text{ T}<B<4 \text{ T}$, Veyrat et al.³² describe both edges of a ribbon as independent $1 G_0$ ballistic conductors (Ref. ³², Eq. 1). Young et al.⁸ find similar behavior caused by applying a canted magnetic field (Ref. ⁸, Eq.1). The effects are explained in terms of gapped graphene with quantum Hall edge states that vanish near zero field, clearly at odds with what we observe. Furthermore away from CNP, in large magnetic fields, these Hall bars exhibit the conventional quantum Hall properties. Hence, the physics involved there^{8,32} does not apply to the EGES. Similarly, the guided edge modes observed by Allen et al.³⁴ at $T=10 \text{ mK}$, on proximity-coupled small neutral exfoliated graphene flakes on BN substrates are not related to the edge states reported here. On similar samples, Marguerite et al. ³¹ found that negative high charge density on the disordered edges produces counter-propagating channels at the edge, which cause

unexpected dissipation at the edge in the quantum Hall regime. Again, these edge states are not related to the EGES.

The EGES in future electronics

Regardless of the physics of the epigraphene edge state, its remarkable insensitivity to disorder that is an inevitable consequence of nanoprocessing, its exceptionally large mean free paths, and the possibility to make integrated structures involving relatively wide ribbons make it relevant not only for fundamental science, but also for future electronics. The N-EG epigraphene structures can be seen as graphene macromolecules consisting of a seamless network of ribbons and junctions; this work is therefore a significant step forward towards realizing new macromolecular device concepts and integrated circuits based on the EGES.

Along those lines, Wakabayashi³⁵ found that a narrow top gate (and also a side gate, Fig. S15) draped over a ribbon can control the edge state current by resonant reflections. Baringhaus et al³⁶ found non-linear, quantum coherent responses in sidewall ribbons supplied with narrow constrictions (Fig. S13), indicating the feasibility of gate controlled resonant tunneling junctions. Recent spin valve measurements³⁷ (Fig. S14) strongly support that the edge state is spin polarized as indicated by the single channel transport, and as theoretically predicted.^{27,38-40} This implies that spintronics applications are feasible. Moreover, the quantum dot properties of the junctions at CNP can be used to route the ballistic current through them, noting that at CNP a junction of size $d[\text{nm}]$ is in its ground state for temperatures $T[\text{K}] < \frac{20,000}{d[\text{nm}]}$. This suggests that the transport properties can be

controlled with potentials $V_c[V] > \frac{2}{d[nm]}$, i.e. about 100 mV for $d=20$ nm, which matches size scales that have been realized with polar epigraphene nanostructures.²⁰

In addition, phase coherent electronics is imminently possible in epigraphene nanostructures. Fabry Perot-like interference effects^{41,42} are observed and an analysis shows that phase coherence length of the EGES is at least 10 μm at $T=4$ K (Fig. S10, S11), which is consistent with bulk epigraphene measurements³. Extrapolating τ_ϕ from Ref.⁴³, the overall size limits L_c for coherent structures are, $L_c=10$ μm , 2 μm , 400 nm and 130 nm, at $T=4$ K, 20 K, 100 K and 300 K, respectively, indicating that even at room temperature coherent epigraphene edge state devices are in principle feasible. Quantum coherence in ballistic 1D devices adds new dimensions to future nanoelectronics that are not accessible with conventional solid-state electronics.

Ballistic transport in sidewall ribbons

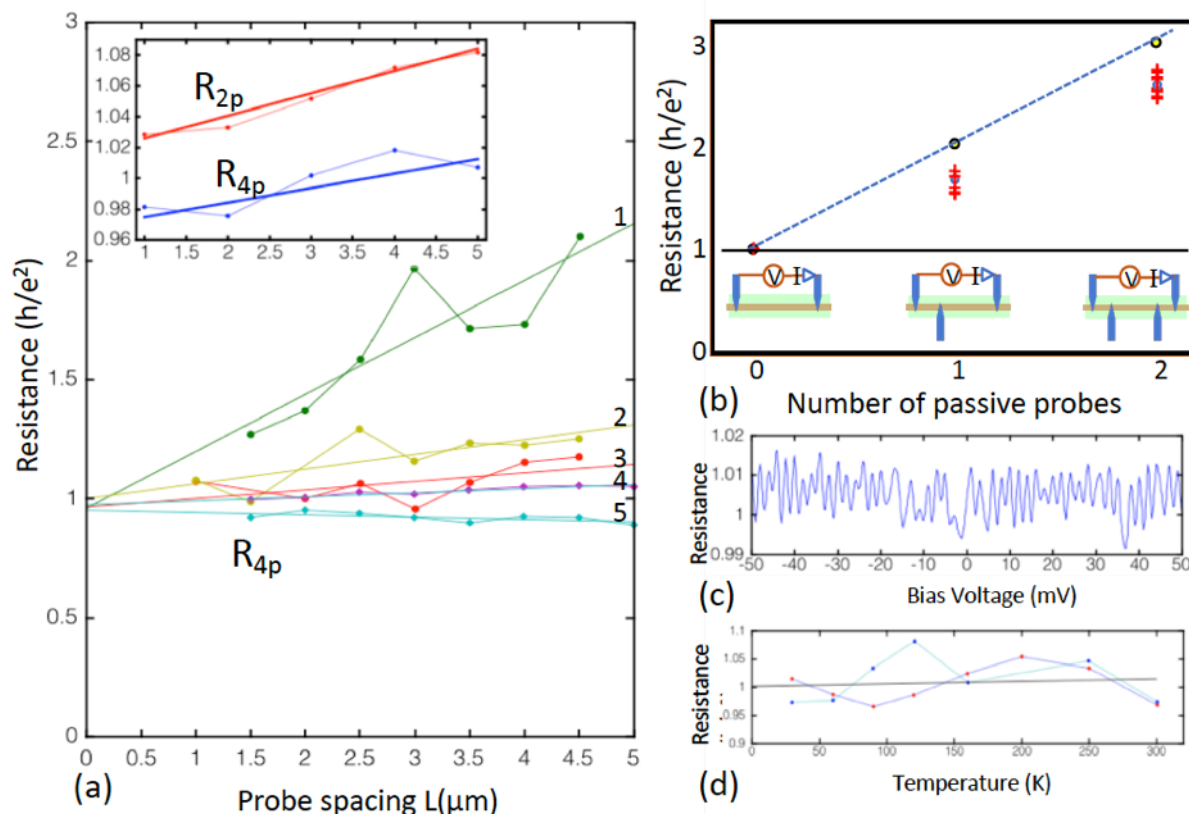


Figure S2. Multi probe in-situ transport measurements of several 40 nm wide graphene sidewall ribbons (adapted from Ref. 1). **(a)** Resistances as a function of probe spacing L conditions. Linear fits extrapolate to $1 R_0$ within a few percent at $L=0$. Slopes from 1 to 5 correspond to mean free paths $\lambda = 4.2, 28, 16, 58, >70 \mu\text{m}$, respectively. (Inset) Sidewall ribbon with $\lambda = 106 \mu\text{m}$; two-point measurement (red) and 4-point measurement (blue) differ by (only) 4%, indicating a probe contact resistance $\approx 500 \Omega$. **(b)** Segmentation of a sidewall ribbon caused by scattering at non-current carrying passive probes placed on the ribbon. A single non-current carrying passive probe, approximately doubles the 2-point resistance of sidewall ribbon. Two passive probes approximately triple the resistance. **(c)** Resistance as a function of bias voltage V_b showing essentially no effect for $-50 \text{ mV} \leq V_b \leq 50 \text{ mV}$ **(d)** Resistance as a function of temperature for two $5 \mu\text{m}$ long ribbons.

Structural and spectroscopic characterization monolayer N-EG

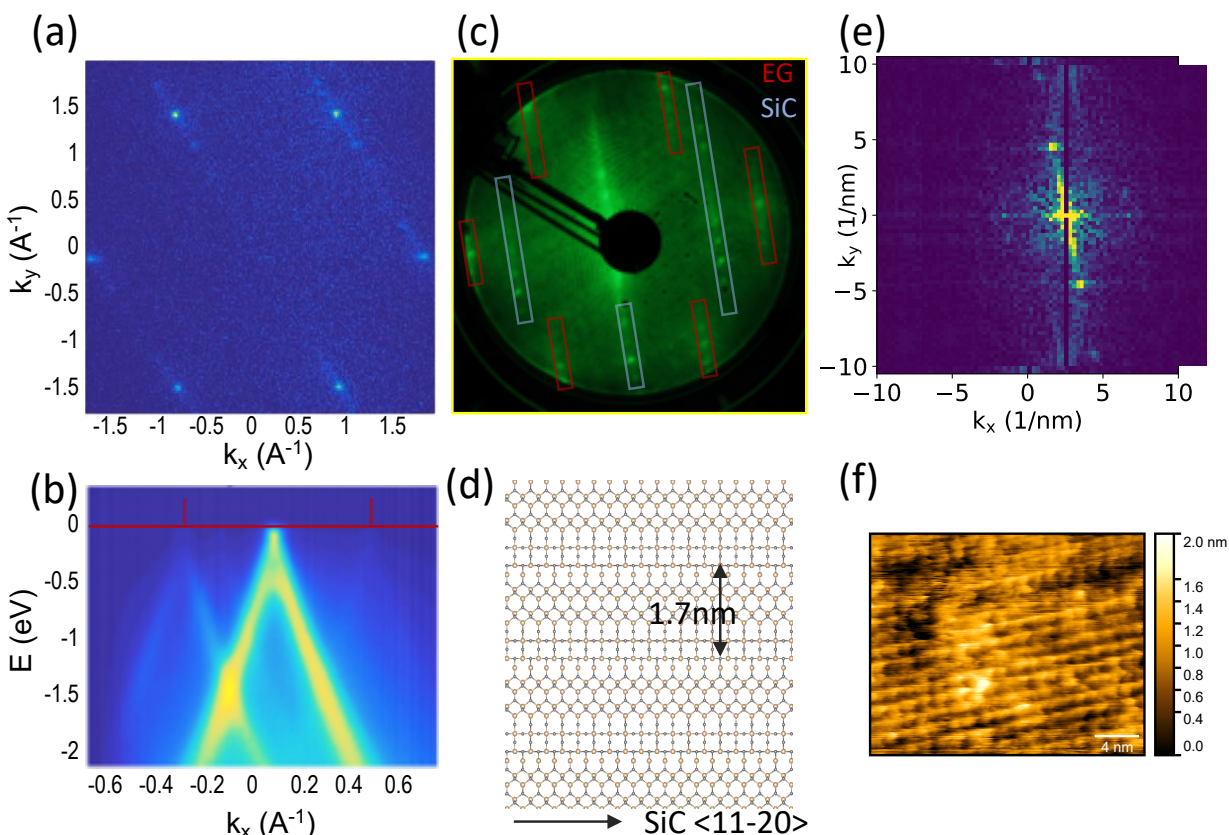


Figure S3. Sample C used in the work presents characteristics of monolayer graphene, with a Raman 2D peak at 2758 cm^{-1} ($\lambda_{\text{laser}}=532\text{ nm}$) that may indicate interaction with the substrate. **(a)** Fermi surface measured in ARPES at room temperature at $E=0\text{ eV}$ (Beam energy 200 eV , $E_F=197.4\text{ eV}$), showing the expected hexagonal Brillouin zone for graphene. Notably, no distortion of the Brillouin zone is observed. The Dirac point is at E_F ; replicas are observed in one direction only, with periodicity $0.4\pm 0.01\text{ \AA}^{-1}$, consistent with LEED. Note that here the k_x axis is oriented 30° from the $<11-20>$ SiC direction shown in (d). **(b)** Energy vs k_x map at $k_y=-1.624\text{ \AA}^{-1}$ (Beam energy= 3 eV , $E_F=32.1\text{ eV}$); the sample was rotated so that the k_x axis is now oriented along the replica dots, that is perpendicularly to the $<11-20>$ SiC direction shown in (d). The plot shows the linear graphene dispersing band and the Dirac point at $E_F=0$ (red line) and two (faint) replica band on each side (red arrows). **(c)** LEED pattern ($E=73\text{ eV}$) showing the graphene (outlined by red

rectangles) and SiC (outlined by blue rectangles) diffraction spots. Rectangles are oriented perpendicularly to the $\langle 11-20 \rangle$ SiC direction shown in (d). Replica spots aligned with the graphene indicate uniaxial modulation of the graphene by the substrate. The spot separation $\Delta k = 0.39 \pm 0.02 \text{ \AA}^{-1}$ agrees with ARPES. **(d)** Example of bulk-cut structure of the top layers of 4H-Si, here for the (1-105) facet, that presents a periodicity of 1.7 nm perpendicular to the $\langle 1-105 \rangle$ direction. **(e)** Fast Fourier transform of the STM image in (f) showing two main peaks corresponding to a modulation of periodicity $1.3 \pm 0.26 \text{ nm}$. **(f)** STM image (bias voltage = 90 mV, $I_{sp} = 900 \text{ pA}$). The parallel set of lines is along the $\langle 1-10n \rangle$ direction, as expected from a substrate structure such as the one shown in (d).

Sample structure and dimensions

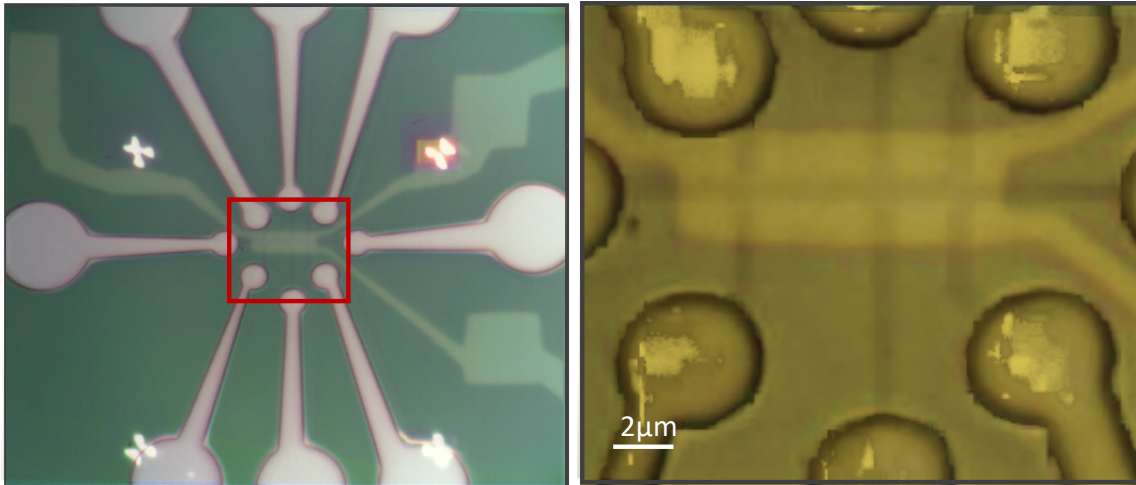


Figure S4. *Picture of device in main text.* (left) Optical image. The picture is a superposition of an image taken before gate deposition, with the resist still on to outline the geometry of the epigraphene Hall bar, and an image after gate deposition, when the device is completed. (Right) contrast enhanced zoom of the red square in the left image.

Longitudinal single segment resistances

Configuration	Segment	Longitudinal resistance (R_0) at $B=9T$, $T=4.5K$
R0C,01	A(top)	1.17
R04,01'	A(bottom)	1.19
R0C,1C	B(top)	1.3
R0C,1'C	B(bottom)	1.3
R11',01	E(left)	0.97
R11',1C	E(right)	1.0
R24,21	F(left)	1.09
R22',23	F(right)	1.28
R04,34	D (top)	1.19
R11',1'C	H(right)	1.05
R11',01'	H(left)	1.0
R22',1'2'	I(left)	1.1

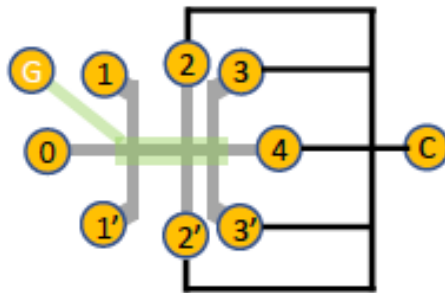


Table 1. Longitudinal single segment resistances, measured at CNP for $B=\pm 9$ T, at $T=4.5$ K. Contact C consists of contacts 2, 2', 3, 3' and 4 mutually connected.

Determination of the charge density from the gate voltage

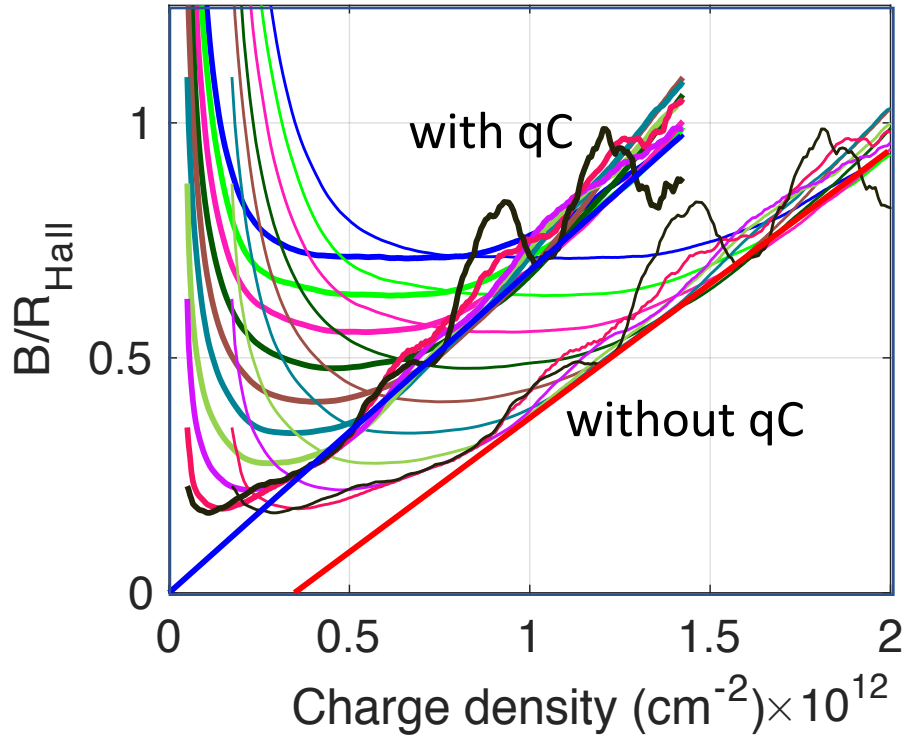


Figure S5. Empirical determination of the quantum capacitance (QC) from $B/R_{\text{Hall}}(n, B_i)$ for various B_i ; $B_i=1$ T (red) to 9 T (blue) and 0.5 T (black). Light lines: without QC so that n is proportional to V_g ($V_g=ne/C$, where C is the classical capacitance per unit area); bold lines: with QC correction, where the bulk charge density n is derived from the top gate potential $V_g=ne(1/C + 2/C_q)$, with $C_q=2ne^2/E_F$ is the quantum capacitance^{44,45}, which we experimentally measured. The empirical QC correction is found to be 2.5 times the theoretical value, indicating a reduced density of states due to the bulk bands at CNP.

Temperature dependence of the conductance

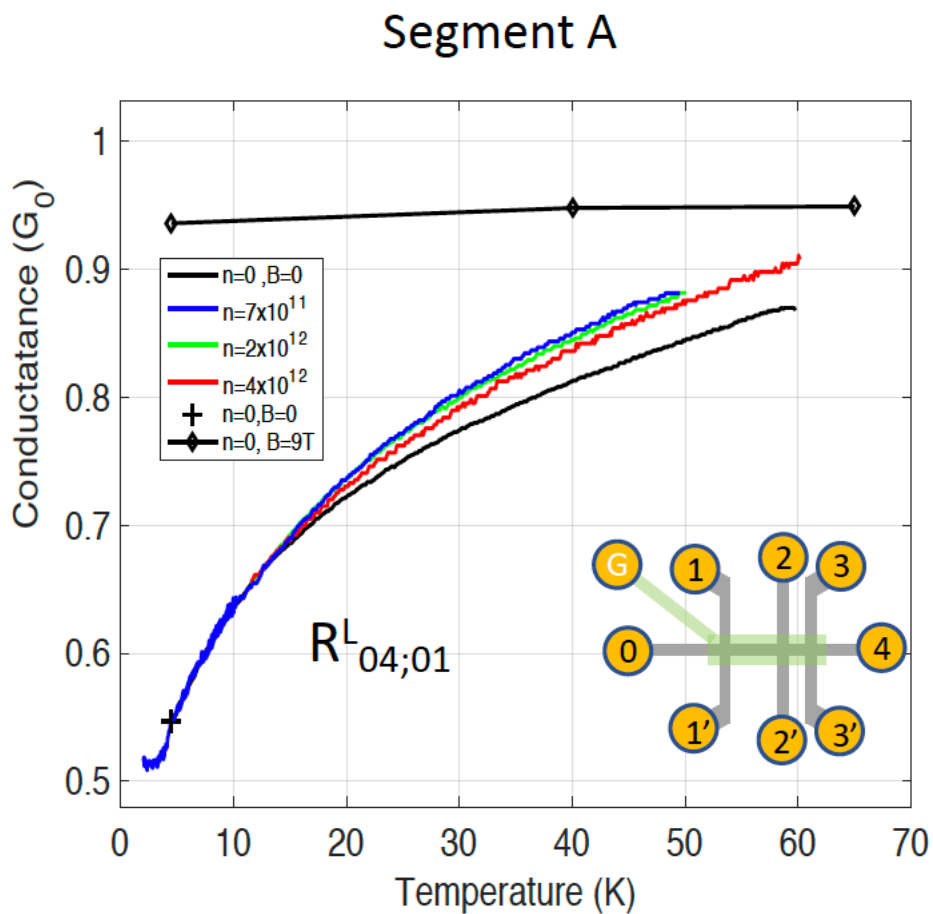


Figure S6. Temperature dependence of segment A (see Fig. 4, main text). Measurements of $G_{04,01}^L$ ($T, B=0, n_i$) for $n=7 \times 10^{11} \text{ cm}^{-2}$ (blue), $n=2 \times 10^{12} \text{ cm}^{-2}$ (green), and $n=4 \times 10^{12} \text{ cm}^{-2}$ (red) that are rigidly shifted to coincide with $G_{04,01}^L$ ($T=4.5 \text{ K}, B=0, n=0$). The curves show good mutual overlap for all T , consistent with Eq. 1. Also shown $G_{04,01}^L$ ($T, B=9 \text{ T}, n=0$), (black diamonds), that is substantially temperature independent (applied current = 1 nA to avoid heating).

Bulk conductivity and mobility

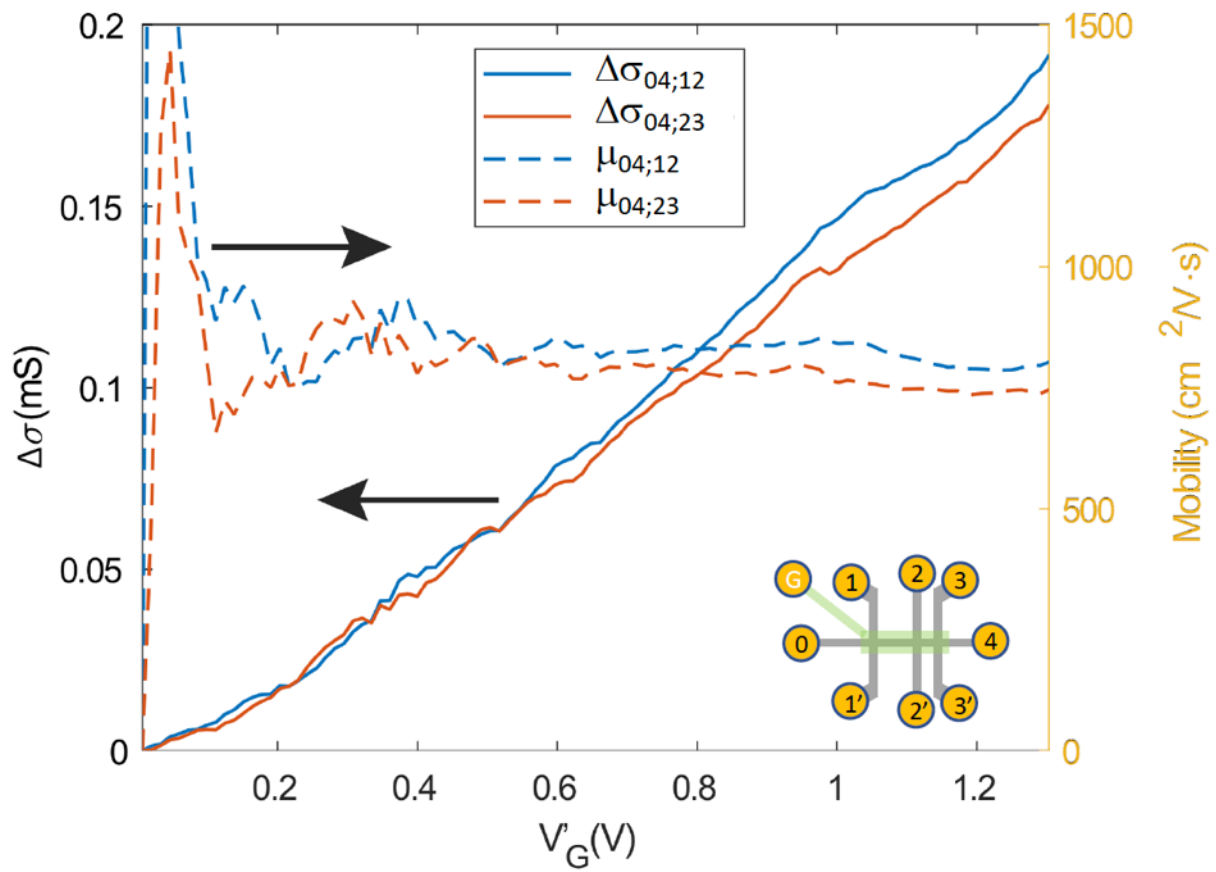


Figure S7. Bulk conductivities and mobilities of segments **B** and **C** vs. gate voltage V_G at $T=12$ K and $B=0$ T (see Fig. 4, main text). The bulk conductivity is $\Delta\sigma = (G(V_G) - G(V_{G=0})) \frac{L}{W}$, where L and W are the segment length and width (Eq.1, main text). The conductivity increases linearly with V_G indicating about constant mobility. Mobilities μ are determined from $\Delta\sigma = n_c e \mu$, where n_c is the gate induced charge density.

Decomposition of the longitudinal conductance of segment A at 3 temperatures

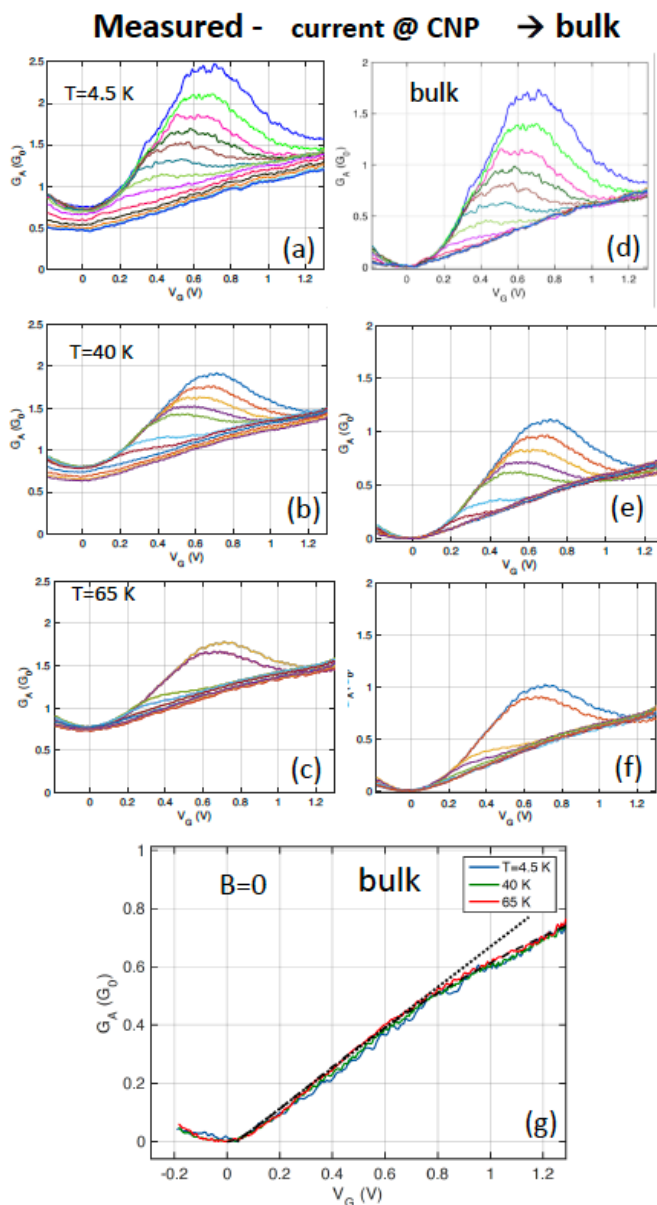


Figure S8. Longitudinal conductance for $T= 4.5$ K **(a,d)**; $T=40$ K **(b,e)**; $T=65$ K **(c,f)** and $B=\pm[9 \dots 1, 0.5, 0.25, 0]$ T, before **(a,b,c)** and after **(d,e,f)** subtraction of the conductance at CNP ($V_G=0$), showing good overlap for $|B|<2$ T over the entire V_G range. This shows that the edge state conductance adds uniformly to the bulk conductance as explained in the main text. **(g)** In addition, the essentially perfect overlap of the $B=0$ bulk conductances for these three temperatures, shows that the temperature dependence of the bulk component is very small, at least up to $T=65$ K. Hence the

measured low-T temperature dependence is entirely due to the edge state, which is due to weak localization as explained in the main text. Note that the reduction of the Shubnikov-de Haas oscillation with increasing temperature is consistent with a graphene monolayer (see Fig. S1). Also shown is the predicted conductance assuming a mobility of $750 \text{ cm}^2/\text{Vs}$ and taking into account that a portion of Segment A is ungated with a charge density of $2 \times 10^{12} \text{ cm}^{-2}$ (dashed line). The dotted line is the predicted conductance assuming that the entire ribbon is gated.

Hall effect at 4K, 40K and 65K

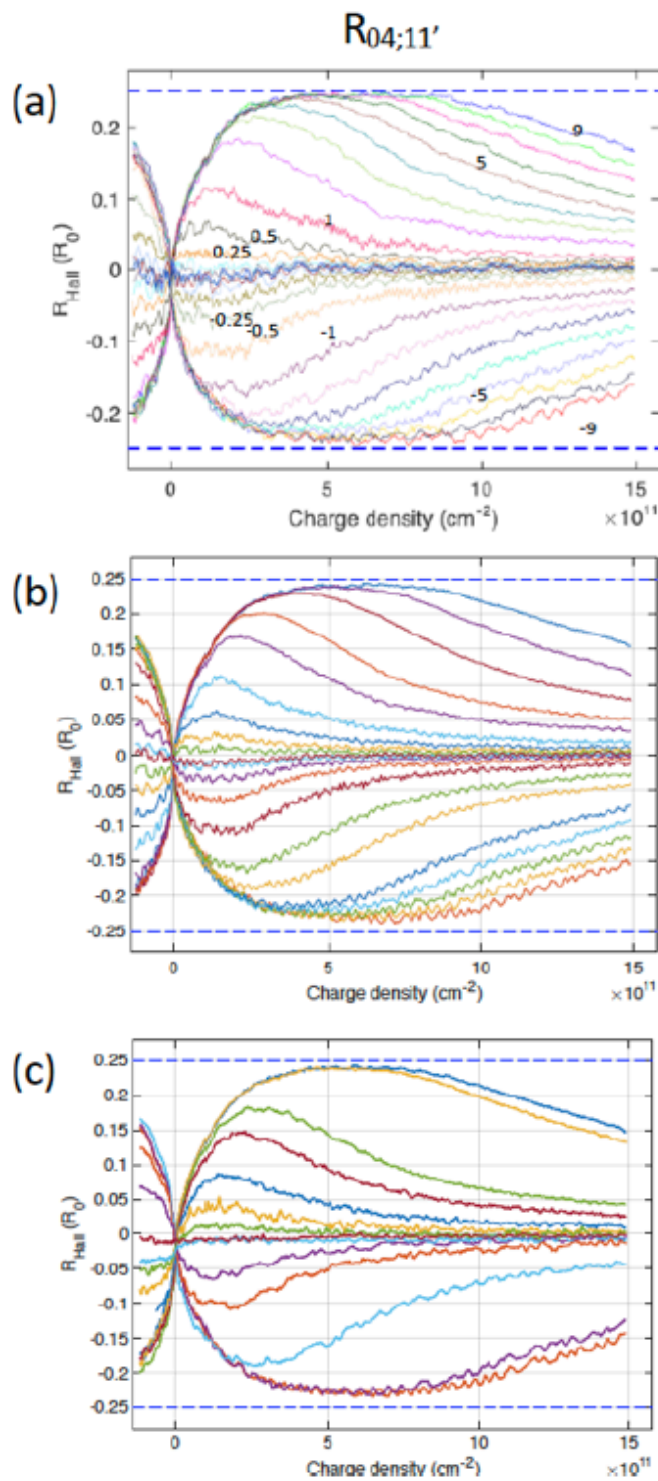


Figure S9. Hall resistance ($R^{\text{Hall}}=R_{04;11'}$).

Hall resistance ($R^{\text{Hall}}=R_{04,11}$) for $T= 4.5\text{K}$ (**a**); $T=40\text{K}$ (**b**); $T=65\text{K}$ (**c**) and $B=\pm[9 \dots 1, 0.5, 0.25, 0]$ T. Positive B gives positive Hall and corresponding colors identifies $G^{L_{04,01}}$. Negative B gives negative Hall and corresponding color identifies $G^{L_{04,01}}$. Note that $G^{L_{04,01}}$ and $G^{L_{04,01}}$ overlap well. Note the reduction in the amplitude of the magneto-conductance maximum (Shubnikov-de Haas oscillation) with increasing temperature, and the vanishing of the weak localization conductance decrease with increasing temperature that is independent of charge density, thereby causing the small conductances for small B to overlap at the higher temperatures.

Correlated resistance fluctuations at the top and bottom edges of segment A

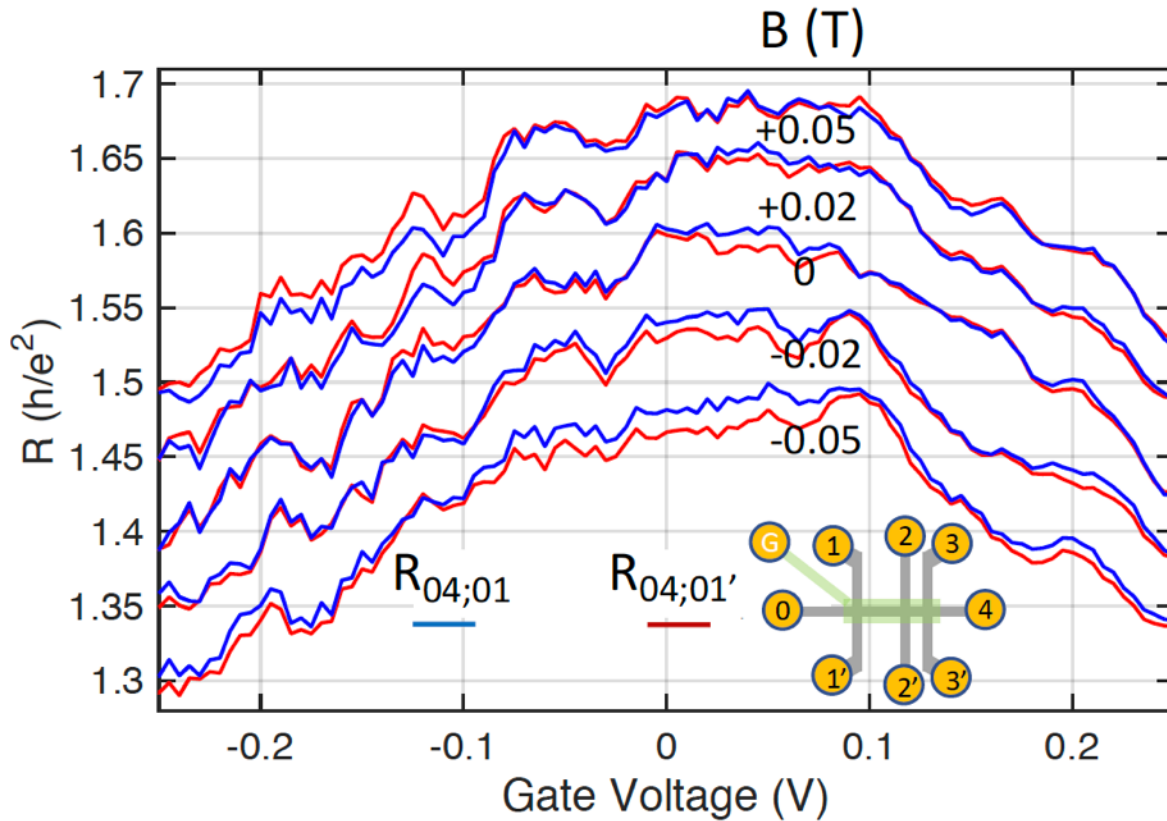


Figure S10. Measured non-symmetrized resistances of opposite sides of Segment A near CNP ($R_{04;01}$ and $R_{04;01'}$), hence the resistance of the EGES for various magnetic fields, clearly showing that the resistances on either side are identical. The fluctuations are not due to current fluctuations, and the red and blue measurements were not performed simultaneously. Successive pairs of traces are displaced by $0.05 h/e^2$ for clarity. This shows that the transport on both sides of the ribbon is correlated. Also note the $\Delta R \approx 0.3 R_0$ departure from $1 R_0$, which is due to a combination of weak localization and the finite mean free path, as explained in the main text.

Coherence of the EGES

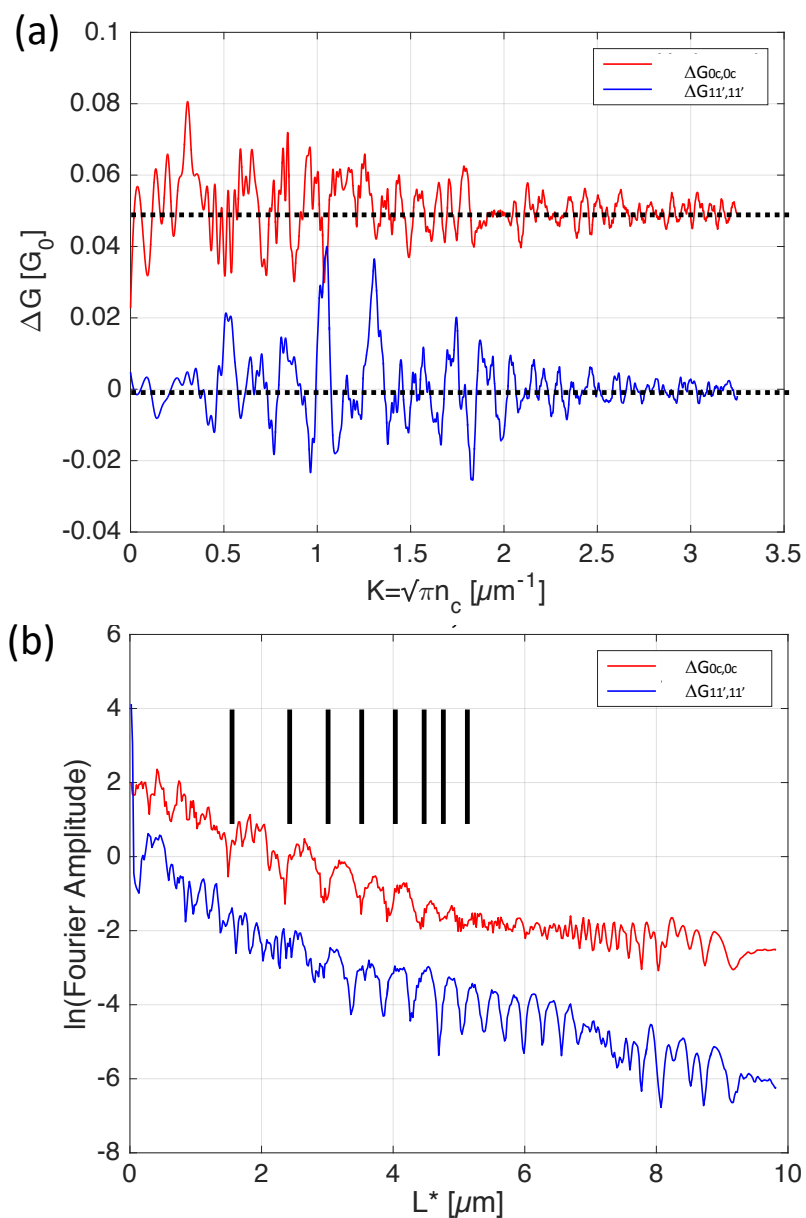


Figure S11. (a) Conductance fluctuations of segments **E+H** ($\Delta G_{11',11'}$, blue) and **A+B** ($\Delta G_{0c,0c}$ red, displaced by $0.05 G_0$) versus bulk wave number k ($k = \sqrt{n_c} \pi$). (b) The corresponding Fourier transform (power spectrum) versus $L^* = 2\pi/k$, presents significant structure. This indicates longitudinal (Fabry-Perot) resonances, indicating phase coherence in the segments due to the EGES. Resonances are seen at all gate voltages and magnetic fields (Fig. S12) Note however that the

resonance sequences are not equally spaced, presumably due to the k dependent Fermi velocity of the EGES, as is expected for edge states^{27,46,47}. Fabry-Perot resonances indicate that at 4.5 K the phase coherence length of the EGES is at least twice the segment lengths, i.e. $> 10 \mu\text{m}$. This is consistent with measured phase coherent times in epigraphene, indicating that low temperature phase coherent epigraphene integrated circuits at $10 \mu\text{m}$ lengths scales are feasible.

EGES Fabry-Perot resonances

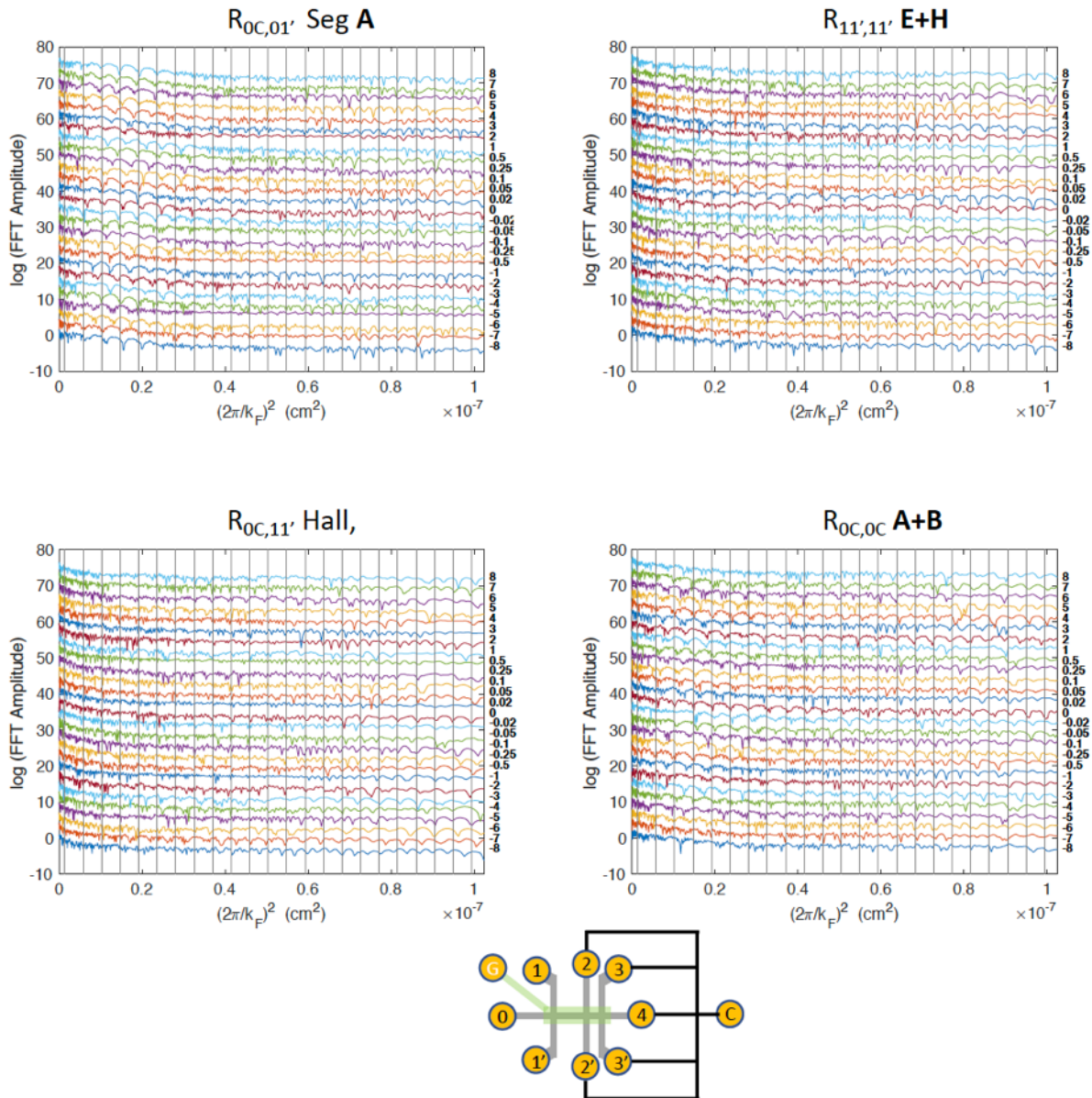


Figure S12. Logarithm of the amplitude of the Fourier transform of $R_{ij,kl}(B_i, k_F)$, plotted versus $(2\pi/k_F)^2$, $k_F = \sqrt{\pi n_C}$, (similar to Fig. S11, but for different configurations, as indicated). The spectra are shifted vertically, and the B_i (in Tesla, from -8 T to +8 T) are indicated at the right border. Note the regular sequences of resonances that are periodic in $1/k_F^2$. Further note that the features remain in the quantum Hall regime and qualitatively appear not to be significantly affected by large magnetic fields.

Sidewall ribbon constrictions

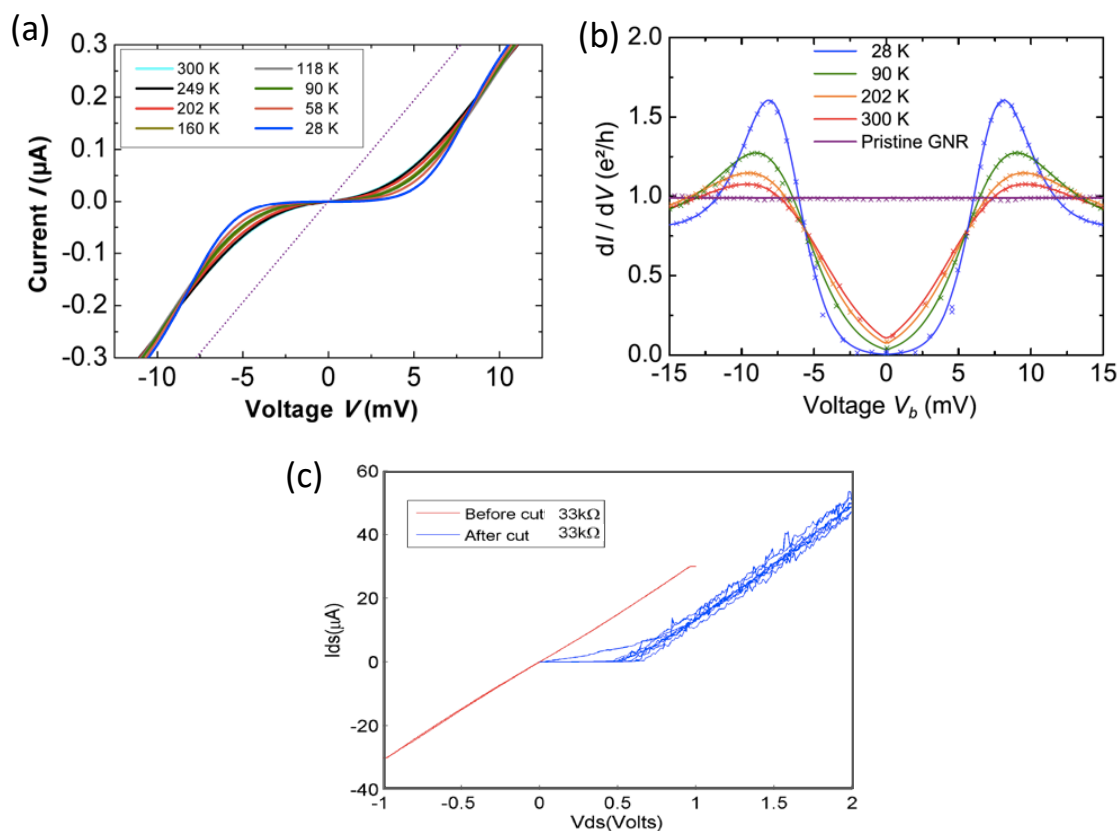


Figure S13. (a) IV curves of a sidewall constriction (length 6 nm and width 2 nm) for different temperatures. The IV of the pristine sidewall GNR is shown for comparison as dotted purple line (reproduced from Refs.36,48). (b) Differential conductance of the IV curve shown in (a). Conductance peaks are clearly visible for the complete temperature range. The purple curve is the differential conductance of the pristine ribbon (from Refs. 36,48) (c) dc-IV characteristics of a sidewall ribbon, before (red) and after the ribbon is physically cut with a SiN AFM tip in ambient conditions (from Ref. 49). Remarkably, the original $33\text{k}\Omega$ resistance of the graphene nanoribbons, measured in ambient condition before cutting, is recovered after cutting. This indicates tunneling across the physical gap, and almost no electronic backscattering at the junction (that would double the resistance as in Ref. 1, Fig 3b).

Epigraphene ribbon spin polarized transport

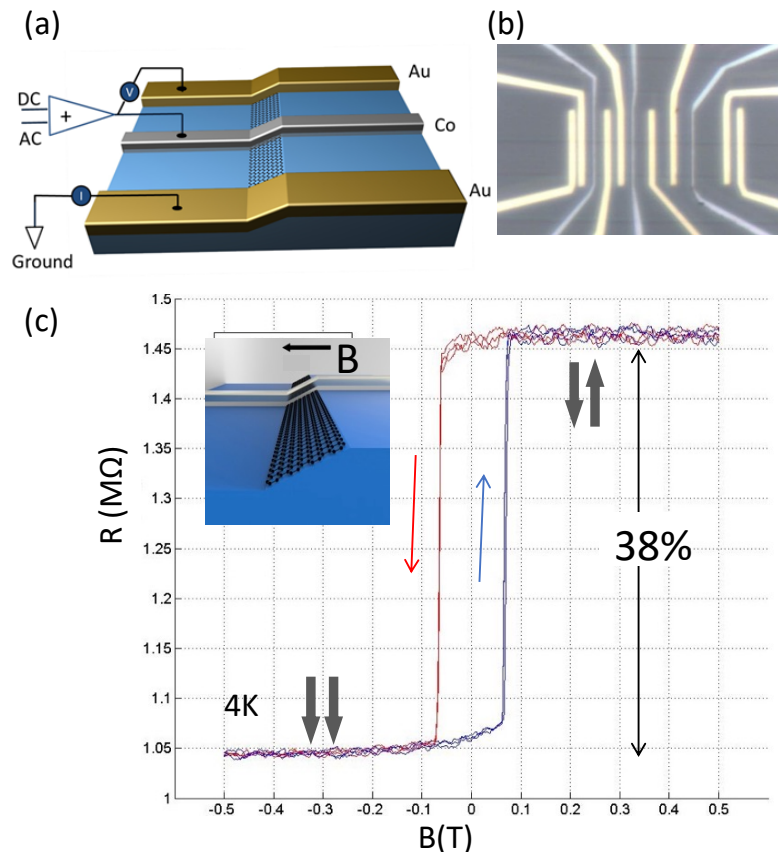


Figure S14. Epigraphene ribbon spin polarized transport (adapted from Refs. 37, 50).

(a) Schematics of a three terminal non-local device, including a slopping epigraphene sidewall nanoribbon connected with a single spin polarizing tunnel contact (Cobalt on Alumina) and two Pd/Au contacts. An AC+DC voltage is applied between the tunnel contact and a Pd/Au contact, where current is measured, while the non-local voltage is measured on the opposing Pd/Au contact.

(b) Optical image of a multi-terminal device (grey: Co/Al₂O₃, gold: Pd/Au). **(c)** Reproducible non local tunnel resistance (2mV AC and 8mV DC applied) showing switching between a high and a low resistance value as the cobalt magnetization is reversed by aligning with the applied magnetic field. The hysteresis is expected for a Cobalt magnetic polarizer. The magnetic field is oriented parallel to the basal (0001) plane, as indicated in the diagram (inset). Note that a single resistance jump is observed, indicating magnetization of the ribbon itself.

Prediction of electronic conductance in graphene ribbons with side-gates

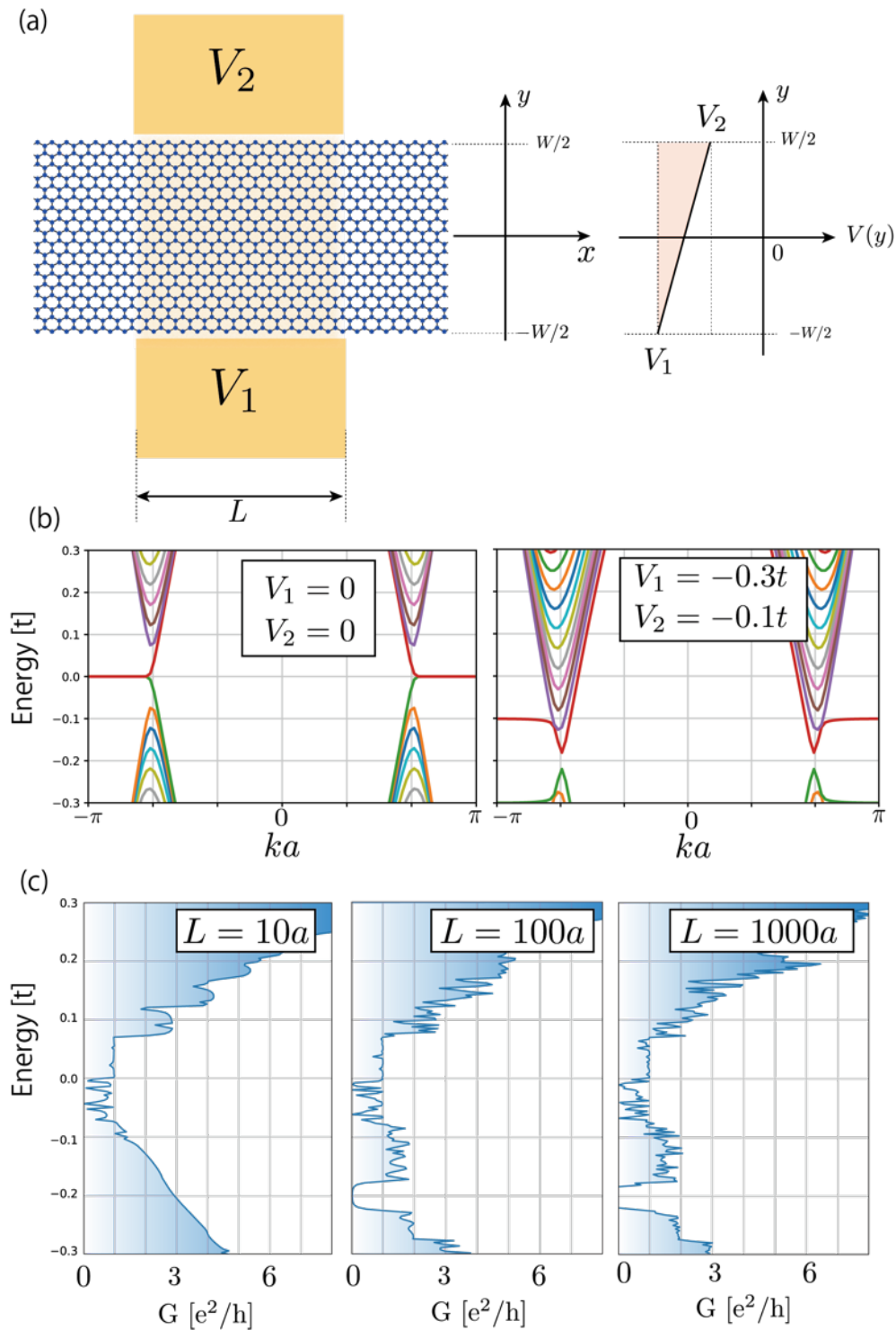


Figure S15. Theoretical calculations for electronic conductance of graphene ribbons with side-gates.

Theoretical calculations for electronic conductance of graphene ribbons with side-gates on the basis of nearest-neighbor tight-binding model, showing that the quantum interference based top-gating effect of the edge state, found in Ref. 35 also applies to side gates (a) Schematic setup of graphene ribbons with side gate. The transverse electric field is locally applied by using side gates, where lower and upper gates have bias voltages of V_1 and V_2 , respectively. In this model, the linear slope potential with $V(y) = \left[\frac{(V_2 - V_1)}{W} y + \frac{V_1 + V_2}{2} \right] t$ is included. Here $t = 2.7$ eV is the transfer integral between nearest-neighbor carbon atoms of tight-binding model, W is the ribbon width and L is the length of side gates. (b) Energy band structure of ribbon with $W = 53a$, where $a = 0.246$ nm is the lattice constant of graphene. (left) Energy band structure in absence of side gate voltage, i.e. $V_1 = V_2 = 0$. Flat bands appear owing to the edge localized states at zero energy. (right) Energy band structure in presence of side gate voltage, i.e. $V_1 = -0.3t, V_2 = -0.1t$. Under side gate bias, the energy bands lift downwards and opening small gap at Dirac cones. (c) Landauer conductance through graphene ribbons with side gate bias for several different length of side gates, i.e. (left) $L = 10a$, (middle) $100a$ and (right) $1000a$. The parameters for side gate bias are $V_1 = -0.3t, V_2 = -0.1t$. Ribbon width $W = 53a$.

References

- 1 Baringhaus, J. *et al.* Exceptional ballistic transport in epitaxial graphene nanoribbons. *Nature* **506**, 349-354, doi:Doi 10.1038/Nature12952 (2014).
- 2 Ruan, M. *Structured epitaxial graphene for electronics* PhD thesis, PhD - Georgia Institute of Technology, (2012).
- 3 Hicks, J. *et al.* A wide-bandgap metal-semiconductor-metal nanostructure made entirely from graphene. *Nature Physics* **9**, 49-54 (2013).
- 4 de Heer, W. A. *et al.* Large Area and Structured Epitaxial Graphene Produced by Confinement Controlled Sublimation of Silicon Carbide. *Proc Nat Acad Sci* **108**, 16900-16905, doi:DOI:10.1073/pnas.1105113108 (2011).
- 5 Hu, Y. *Graphene on non-polar SiC facets* PhD thesis, PhD - Georgia Institute of Technology, (2020).
- 6 Quaglio, T. *et al.* A subKelvin scanning probe microscope for the electronic spectroscopy of an individual nano-device. *Review of Scientific Instruments* **83**, 123702, doi:10.1063/1.4769258 (2012).
- 7 Han, M. Y., Brant, J. C. & Kim, P. Electron Transport in Disordered Graphene Nanoribbons. *Physical Review Letters* **104**, 056801 (2010).
- 8 Young, A. F. *et al.* Tunable symmetry breaking and helical edge transport in a graphene quantum spin Hall state. *Nature* **505**, 528-532, doi:10.1038/nature12800 (2014).
- 9 Kosynkin, D. V. *et al.* Longitudinal unzipping of carbon nanotubes to form graphene nanoribbons. *Nature* **458**, 872-876, doi:10.1038/nature07872 (2009).
- 10 Jiao, L. Y., Zhang, L., Wang, X. R., Diankov, G. & Dai, H. J. Narrow graphene nanoribbons from carbon nanotubes. *Nature* **458**, 877-880, doi:Doi 10.1038/Nature07919 (2009).

- 11 Poumirol, J.-M. *et al.* Edge magnetotransport fingerprints in disordered graphene nanoribbons. *Physical Review B* **82**, 041413, doi:10.1103/PhysRevB.82.041413 (2010).
- 12 Gallagher, P., Todd, K. & Goldhaber-Gordon, D. Disorder-induced gap behavior in graphene nanoribbons. *Physical Review B* **81**, 115409 (2010).
- 13 Stampfer, C. *et al.* Energy Gaps in Etched Graphene Nanoribbons. *Physical Review Letters* **102**, 056403 (2009).
- 14 Sols, F., Guinea, F. & Neto, A. H. C. Coulomb Blockade in Graphene Nanoribbons. *Physical Review Letters* **99**, 166803, doi:10.1103/PhysRevLett.99.166803 (2007).
- 15 Libisch, F., Rotter, S. & Burgdörfer, J. Coherent transport through graphene nanoribbons in the presence of edge disorder. *New J Phys* **14**, 123006, doi:10.1088/1367-2630/14/12/123006 (2012).
- 16 Plasser, F. *et al.* The Multiradical Character of One- and Two-Dimensional Graphene Nanoribbons. *Angew Chem Int Edit* **52**, 2581-2584, doi:10.1002/anie.201207671 (2013).
- 17 Zhang, X. W. *et al.* Experimentally Engineering the Edge Termination of Graphene Nanoribbons. *Acs Nano* **7**, 198-202, doi:10.1021/nn303730v (2013).
- 18 Bellunato, A., Arjmandi Tash, H., Cesa, Y. & Schneider, G. F. Chemistry at the Edge of Graphene. *ChemPhysChem* **17**, 785-801, doi:10.1002/cphc.201500926 (2016).
- 19 Epping, A. *et al.* Insulating State in Low-Disorder Graphene Nanoribbons. *physica status solidi (b)* **256**, 1900269, doi:https://doi.org/10.1002/pssb.201900269 (2019).
- 20 Hwang, W. S. *et al.* Graphene nanoribbon field-effect transistors on wafer-scale epitaxial graphene on SiC substrates. *APL Materials* **3**, 011101, doi:10.1063/1.4905155 (2015).

- 21 Palacio, I. *et al.* Atomic Structure of Epitaxial Graphene Sidewall Nanoribbons: Flat Graphene, Miniribbons, and the Confinement Gap. *Nano Lett* **15**, 182–189, doi:10.1021/nl503352v (2015).
- 22 Norimatsu, W. & Kusunoki, M. Growth of graphene from SiC{0001} surfaces and its mechanisms. *Semicond Sci Tech* **29**, 064009, doi:10.1088/0268-1242/29/6/064009 (2014).
- 23 Pereira, J. M., Peeters, F. M. & Vasilopoulos, P. Landau levels and oscillator strength in a biased bilayer of graphene. *Physical Review B* **76**, 115419, doi:10.1103/PhysRevB.76.115419 (2007).
- 24 Kou, A. *et al.* Electron-hole asymmetric integer and fractional quantum Hall effect in bilayer graphene. *Science* **345**, 55-57, doi:10.1126/science.1250270 (2014).
- 25 Lifshitz, I. M. & Kosevich, A. M. Theory of Magnetic Susceptibility in Metals at Low Temperatures. *Soviet Physics JETP* **2**, 636 (1955).
- 26 Berger, C. *et al.* Electronic confinement and coherence in patterned epitaxial graphene. *Science* **312**, 1191-1196 (2006).
- 27 Wakabayashi, K., Fujita, M., Ajiki, H. & Sigrist, M. Electronic and magnetic properties of nanographite ribbons. *Physical Review B* **59**, 8271-8282 (1999).
- 28 Tzalenchuk, A. *et al.* Towards a quantum resistance standard based on epitaxial graphene. *Nat Nanotechnol* **5**, 186-189 (2010).
- 29 Ribeiro-Palau, R. *et al.* Quantum Hall resistance standard in graphene devices under relaxed experimental conditions. *Nat Nanotechnol* **10**, 965-U168, (2015).
- 30 Wu, X. S. *et al.* Half integer quantum Hall effect in high mobility single layer epitaxial graphene. *Appl Phys Lett* **95**, 223108 (2009).

- 31 Marguerite, A. *et al.* Imaging work and dissipation in the quantum Hall state in graphene. *Nature* **575**, 628-633, doi:10.1038/s41586-019-1704-3 (2019).
- 32 Veyrat, L. *et al.* Helical quantum Hall phase in graphene on SrTiO₃. *Science* **367**, 781-786, doi:10.1126/science.aax8201 (2020).
- 33 Brey, L. & Fertig, H. A. Edge states and the quantized Hall effect in graphene. *Physical Review B* **73**, 195408, doi:10.1103/PhysRevB.73.195408 (2006).
- 34 Allen, M. T. *et al.* Spatially resolved edge currents and guided-wave electronic states in graphene. *Nature Physics* **12**, 128-133, doi:10.1038/Nphys3534 (2016).
- 35 Wakabayashi, K. & Aoki, T. Electrical conductance of zigzag nanographite ribbons with locally applied gate voltage. *Int J Modern Physics B* **16**, 4897-4909, doi:10.1142/s0217979202014917 (2002).
- 36 Baringhaus, J. *et al.* Electron Interference in Ballistic Graphene Nanoconstrictions. *Physical Review Letters* **116**, 186602, doi:10.1103/PhysRevLett.116.186602 (2016).
- 37 Hankinson, J. *Spin dependent current injection into epitaxial graphene nanoribbons* PhD thesis, PhD - Georgia Institute of Technology, (2015).
- 38 Li, J., Niquet, Y.-M. & Delerue, C. Magnetic-Phase Dependence of the Spin Carrier Mean Free Path in Graphene Nanoribbons. *Physical Review Letters* **116**, 236602, doi:10.1103/PhysRevLett.116.236602 (2016).
- 39 Yazyev, O. V. Emergence of magnetism in graphene materials and nanostructures. *Reports on Progress in Physics* **73**, 056501(056516pp) (2010).
- 40 Magda, G. Z. *et al.* Room-temperature magnetic order on zigzag edges of narrow graphene nanoribbons. *Nature* **514**, 608-611, doi:10.1038/nature13831 (2014).

- 41 Liang, W. J. *et al.* Fabry-Perot interference in a nanotube electron waveguide. *Nature* **411**, 665-669 (2001).
- 42 Jiao, L. Y., Wang, X. R., Diankov, G., Wang, H. L. & Dai, H. J. Facile synthesis of high-quality graphene nanoribbons. *Nat Nanotechnol* **5**, 321-325 (2010).
- 43 Eless, V. *et al.* Phase coherence and energy relaxation in epitaxial graphene under microwave radiation. *Appl Phys Lett* **103**, 093103, doi:10.1063/1.4819726 (2013).
- 44 Das, A. *et al.* Monitoring dopants by Raman scattering in an electrochemically top-gated graphene transistor. *Nat Nanotechnol* **3**, 210-215, doi:10.1038/nnano.2008.67 (2008).
- 45 Fang, T., Konar, A., Xing, H. L. & Jena, D. Carrier statistics and quantum capacitance of graphene sheets and ribbons. *Appl Phys Lett* **91**, 092109, doi:Artn 092109 10.1063/1.2776887 (2007).
- 46 Fujita, M., Wakabayashi, K., Nakada, K. & Kusakabe, K. Peculiar localized state at zigzag graphite edge. *J Phys Soc Jpn* **65**, 1920-1923 (1996).
- 47 Nakada, K., Fujita, M., Dresselhaus, G. & Dresselhaus, M. S. Edge state in graphene ribbons: Nanometer size effect and edge shape dependence. *Physical Review B* **54**, 17954-17961 (1996).
- 48 Baringhaus, J. Mesoscopic transport phenomena in epitaxial graphene nanostructures : a surface science approach. *PhD - dissertation - Leibniz Univ, Hannover* <http://edok01.tib.uni-hannover.de/edoks/e01dh15/839487312.pdf> (2015).
- 49 Palmer, J. *Pre-growth structures for nanoelectronics of EG on SiC* PhD thesis, Georgia Inst. Techn, (2014).
- 50 Huan, C. *et al.* Tunnel magnetoresistance of magnetic junctions based on side-wall epitaxial graphene nanoribbons. *APS March Meeting*, B7.00001 (2013).